

TEMPERATURE AND EXTREME-ULTRAVIOLET INTENSITY IN A CORONAL PROMINENCE CAVITY AND STREAMER

T. A. KUCERA¹, S. E. GIBSON², D. J. SCHMIT^{2,3}, E. LANDI⁴, AND D. TRIPATHI⁵

¹ NASA/GSFC, Code 671, Greenbelt, MD 20771, USA

² HAO/NCAR, P.O. Box 3000, Boulder, CO 80307-3000, USA

³ Department of Astrophysical and Planetary Science, University of Colorado, Boulder, CO 80305, USA

⁴ Department of Atmospheric, Oceanic and Space Science, Space Research Building, University of Michigan, 2455 Hayward St., Ann Arbor, MI 48109-2143, USA

⁵ Inter-University Centre for Astronomy and Astrophysics, Post Bag-4, Ganeshkhind, Pune University Campus, Pune 411 007, India

Received 2012 February 2; accepted 2012 August 2; published 2012 September 5

ABSTRACT

We analyze the temperature and EUV line emission of a coronal cavity and surrounding streamer in terms of a morphological forward model. We use a series of iron line ratios observed with the *Hinode* Extreme-ultraviolet Imaging Spectrograph (EIS) on 2007 August 9 to constrain temperature as a function of altitude in a morphological forward model of the streamer and cavity. We also compare model predictions to the EIS EUV line intensities and polarized brightness (pB) data from the Mauna Loa Solar Observatory (MLSO) Mark 4 K-coronameter. This work builds on earlier analysis using the same model to determine geometry of and density in the same cavity and streamer. The fit to the data with altitude-dependent temperature profiles indicates that both the streamer and cavity have temperatures in the range 1.4–1.7 MK. However, the cavity exhibits substantial substructure such that the altitude-dependent temperature profile is not sufficient to completely model conditions in the cavity. Coronal prominence cavities are structured by magnetism so clues to this structure are to be found in their plasma properties. These temperature substructures are likely related to structures in the cavity magnetic field. Furthermore, we find that the model overestimates the EUV line intensities by a factor of 4–10, without overestimating pB. We discuss this difference in terms of filling factors and uncertainties in density diagnostics and elemental abundances.

Key words: Sun: corona – Sun: filaments, prominences

Online-only material: color figures

1. INTRODUCTION

Coronal cavities are the coronal manifestations of filament channels. They can be seen in cross section at the solar limb above magnetic neutral lines and below brighter coronal streamers. They surround solar prominences and in some models these features share a joint magnetic field. They are observed to erupt, forming the dark cavity in the classical three-part coronal mass ejection (CME) shape of bright front, dark cavity, and bright prominence core (Gibson et al. 2006). Understanding the physical characteristic of cavities, including density and temperature as well as flow patterns and magnetic field, should provide valuable clues to long-standing questions concerning the triggers to CME eruption and the processes involved in the formation and maintenance of prominences.

It has been established that cavities are, as the name implies, less dense than the surrounding streamers. Cavity densities are most unambiguously determined from white-light observations, which are temperature independent, and these indicate a lower limit of approximately half the density of a surrounding streamer at the same height (Fuller & Gibson 2009).

Temperature measurements have proven to be more ambiguous. Efforts have been made using white-light data to infer a density scale height and associated “hydrostatic temperature” (Guhathakurta et al. 1992; Fuller et al. 2008; Fuller & Gibson 2009). These have indicated higher hydrostatic temperatures in the cavity than the streamer. However, these calculations require simplifying assumptions concerning the boundary conditions for cavity and streamer flux tubes (Fuller et al. 2008). Measurements using coronal spectral lines do not require these assumptions and indicate that cavities and, in some studies, streamers are not hydrostatic. The Guhathakurta et al. (1992) white-light

observations were complemented by measurements of coronal red (6374 Å Fe x) and green (5303 Å Fe xiv) lines that indicated that the cavity was cooler than the streamer, contradicting the hydrostatic white-light calculations for the same cavity. Vásquez et al. (2009) used tomographic analysis of streamers and cavities using data from the Extreme Ultraviolet Imager (EUVI) aboard the *Solar Terrestrial Relations Observatory* (STEREO) and found that the cavity temperature distribution was broader and extended to higher temperatures than did those of the surrounding streamers.

Cavities also appear to have internal substructure in temperature and velocity. Hudson et al. (1999) and Reeves et al. (2012) report soft-X-ray emission has been observed surrounded by an otherwise low-emission cavity, and “hot shrouds” around prominences associated with cavities have been observed in visible and IR emission (Habbal et al. 2010). Such hot cores are often but not always present within cavities, and may have a disk-like or ring-like shape (Reeves et al. 2012). They extend to heights well above the prominence, but do not fill the cavity. Further observations of cavity structure include measurements by Wang & Stenborg (2010) and Schmit et al. (2009) who analyzed coherent velocity structures within cavities, in the plane of the sky (POS) and along the line of sight, respectively.

In this analysis we have used a morphological forward model to analyze a cavity and surrounding streamer observed in 2007 August. Because a cavity is an elongated three-dimensional feature embedded in a brighter streamer, it is difficult to directly measure its properties. The emission from a given location in the POS is a combination of different components along the line of sight from various locations in the cavity and streamer. Thus, in order to determine density and temperature we employ forward modeling. In particular, we use a morphological model of the

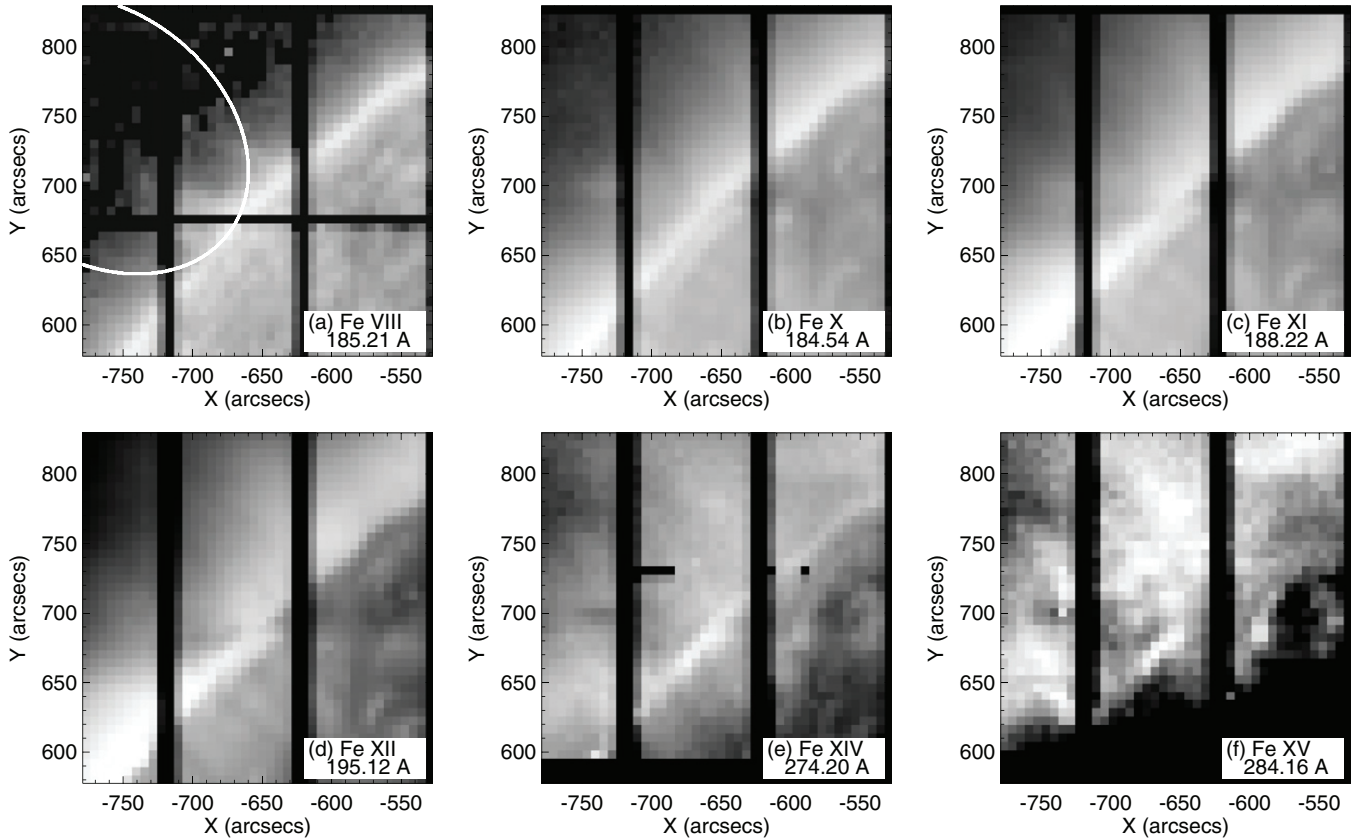


Figure 1. EIS raster images taken on 2007 August 9 from 14:19:20–18:42:30 UT. Intensities are on a log scale. The images have been binned by a factor of six so that each pixel is $6'' \times 6''$. The Fe VIII image (a) is included to show the location of the prominence in emission at transition region temperatures ($\approx 500,000$ K). It is also overlaid with a curve showing the border of the model cavity in the plane of the sky. Other data shown (b–f) are used in our temperature analysis. The dark vertical bands represent the portions of the orbit during spacecraft night.

cavity and streamer with parameterized density and temperature distribution to calculate directly measurable spectral line ratios. By varying the parameters of the model, a best fit to observed line ratios may be found that is an improvement over many earlier efforts that assume a uniform density in all emitting material along the line of sight or hydrostatic equilibrium.

This paper is third in a series. In the first paper (Gibson et al. 2010, Paper I), data from *STEREO*/EUVI were used to determine the morphological parameters of the model in which the cavity is modeled as a long low-density tube of varying cross section in a coronal streamer. Schmit & Gibson (2011, Paper II) then used data from the *Hinode*/Extreme-ultraviolet Imaging Spectrograph (EIS) and the Mauna Loa Solar Observatory Mark 4 K-coronameter (MLSO/Mk4) to forward model both a density-sensitive Fe XII line ratio and white-light data to determine density as a function of altitude in the cavity and the streamer. They found an average density depletion of the cavity relative to the streamer of about 30%.

Here we build on these previous results by using observations of a series of iron lines observed by EIS to forward model the temperature profile in the cavity and streamer. We also compare the extreme-ultraviolet (EUV) intensity values in order to investigate filling factors in the streamer and cavity.

This multi-step approach has allowed us to apply diagnostics that isolate particular model parameters rather than considering all possible variables at once. Thus, in Paper II we used a density-sensitive EUV line ratio to determine density. In this paper, we use a series of temperature-sensitive line ratios to develop model temperature profiles. In this way we can look at the effects of

varying these parameters in relative isolation from the many other factors which can affect EUV intensities.

In the following section we describe the observations and data reduction. In Section 3 we discuss the forward model and the analysis of the data in terms of the model, first discussing the modeling of temperature-dependent line ratios to determine temperature profiles in the cavity and streamer. We then combine this temperature fit with the density and morphology determined in the previous two papers to fully compare data and model line intensities. In Section 4 we discuss possible interpretations of our analysis, and in the final section we summarize our conclusions.

2. DATA AND DATA REDUCTION

This cavity was observed in 2007 August as part of a campaign associated with the International Heliophysical Year. The full set of multi-instrument observations is described in Paper I. The cavity was over a polar crown prominence in the northeast. Rasters from six of the lines observed with EIS are shown in Figure 1. The basic elliptical cavity structure is most clear in the Fe X, Fe XI, and Fe XII raster images. The images produced by the hotter lines, especially Fe XV, show a more complex array of structures. We also show the Fe VIII 185.21 Å raster from EIS and, in Figure 2, He II 304 Å and Fe XII 195 Å band images from the *Solar and Heliospheric Observatory*'s Extreme-ultraviolet Imaging Telescope (*SOHO*/EIT) to show the location of the prominence.

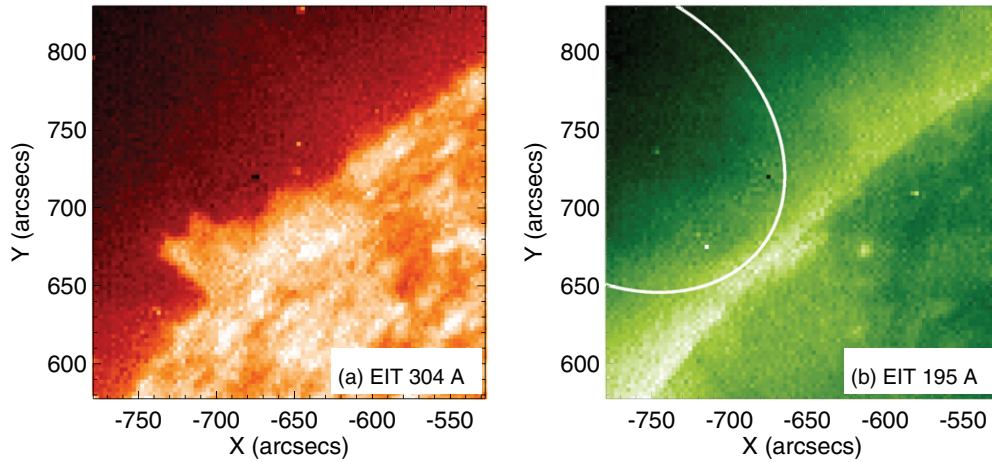


Figure 2. Images from *SOHO*/EIT on 2007 August 9 in (a) the 304 Å band at 18:35:19 UT and (b) the 195 Å band at 13:12:32 UT for comparison with the EIS images in Figure 1. Overlaid on the 195 Å band image is the boundary of the model cavity in the plane of the sky as determined in Paper I.

(A color version of this figure is available in the online journal.)

Table 1
Spectral Lines Used in Temperature Analysis

Ion	λ (Å)	Transition	L1	L2
Fe x	184.54	$3s^2 3p^5 \ ^2P_{3/2} - 3s^2 3p^4 \ (^1D) 3d \ ^2S_{1/2}$	1	27
Fe xi	188.23	$3s^2 3p^4 \ ^3P_2 - 3s^2 3p^3 \ (^2D) 3d \ ^3P_2$	1	38
Fe xii	195.12	$3s^2 3p^3 \ ^4S_{3/2} - 3s^2 3p^2 \ (^3P) 3d \ ^4P_{5/2}$	1	27
Fe xiv	274.20	$3s^2 3p^2 \ ^1P_{1/2} - 3s \ 3p^2 \ ^2S_{1/2}$	1	8
Fe xv	284.16	$3s^2 \ ^1S_0 - 3s \ 3p \ ^1P_1$	1	5

Note. L1 and L2 are the lower and upper atomic energy levels of the transition.

2.1. EIS Fe Line Data

The EIS data used were extracted from the same raster as those used for the density-sensitive line ratio analysis in Paper II. EIS (Culhane et al. 2007) is a slit spectrometer taking data in the ranges 171–212 Å and 245–291 Å, but only selected lines are telemetered down during most observations. The EIS raster was taken from 2007 August 9 14:19:20–18:42:30 UT, with a step size of 1'' and exposure time of 60 s. Pixel size along the slit was also 1''. Original images were $256'' \times 256''$. The data were analyzed with the standard `eis_prep` routines available in SolarSoft (Young et al. 2009; Young 2011). We used the optional correction for CCD degradation over time. This correction led to an increase in intensity values of 18.5% from the uncorrected data. In order to increase signal to noise, the data were binned by a factor of six. Data from different lines were aligned using the EIS routines that correct for pointing shifts as a function of wavelength and then aligned with other data sets using offsets calculated for the work in Paper II.

For our temperature analysis we used a series of lines, listed in Table 1. For densities $\lesssim 10^9 \text{ cm}^{-3}$ the lines are density insensitive beyond the normal n_e^2 dependence of collisionally excited lines from allowed transitions. This minimizes the dependence of their ratios on the model of density developed in Paper II.

2.1.1. EIS Scattered Light

Because cavities are relatively low intensity features, we also attempted to correct the data for stray light contamination. Ugarte-Urra (2010) used data from a partial lunar eclipse of the Sun as seen by *Hinode* to estimate that the stray light component to EIS emission is a minimum of 2% of the average on-disk

emission at a given wavelength. Hahn et al. (2011) used this result when analyzing data in a coronal hole, applying a stray light correction based on 2% of the on-disk values as measured from the portion of their raster that included on-disk data. They checked this method by analyzing on- and off-disk emission from an He II, Si x blend at 256.3 Å and Si x at 261.0 Å, and found that the 2% value seemed reasonable.

We employed a similar method, subtracting a value of 2% of the average disk emission in each line. This is probably larger than the factor used by Hahn et al. because they were using coronal hole data while we were observing adjacent to the quiet Sun. We find that the importance of this correction is highly dependent on the temperature of formation of the line due to the temperature-dependent contrast between disk and off-limb emission. For the Fe x emission, which falls off rapidly with altitude, the correction is about 10% at an altitude of $1.1 R_\odot$ and 35% at an altitude of $1.6 R_\odot$, whereas for the Fe xv emission the correction never exceeds 2%.

2.2. MLSO Mk4

In this paper, we also discuss polarized brightness (pB) data taken by the MLSO/Mk4 Coronagraph Polarimeter (Elmore et al. 2003). These data and their analysis are described in Papers I and II. The Mk4 data for this streamer and cavity extend from 1.17 to $1.50 R_\odot$. The lower limit of this range is slightly higher than that of the EIS data used in our analysis, which extend up to $1.163 R_\odot$ in the cavity and $1.144 R_\odot$ in the streamer (see Section 3.2).

3. ANALYSIS

3.1. Model

In order to more carefully analyze possible line-of-sight effects (for instance, streamer material in the foreground and background of the cavity), we utilize a morphological cavity model. The cavity is modeled as a tunnel-like structure in an elongated streamer with elliptical cross section and a Gaussian variation in height along the tunnel length.

In Paper I, Gibson et al. (2010) determined the dimensions and orientation of the cavity by fitting the shape of the cavity in limb EUV observations of a cavity over the course of several days using different points of view provided by the two *STEREO*

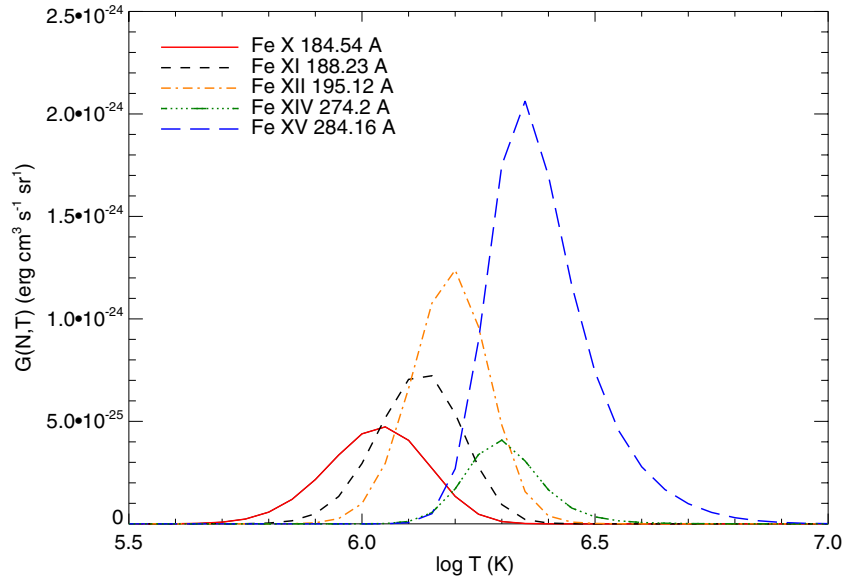


Figure 3. Contribution functions for the lines used in this investigation. These values include elemental abundances and the $n(\text{H})/n_e$ ratio. (A color version of this figure is available in the online journal.)

spacecraft. Paper II also presents slight adjustments to the streamer and cavity geometry, and we include those changes here.

In Paper II, Schmit & Gibson (2011) forward fit the density-sensitive Fe XII line ratio 186.880/195.119 Å and MLSO/Mk4 pB data using separate density profiles for the cavity and streamer. The resulting profiles are described by the equations:

$$n_{\text{estr}} = (1.27r_{\text{piv}}^{-22.8} + 5.97r_{\text{piv}}^{-16.0} + 1.57r_{\text{piv}}^{-3.87}) \times 10^8 \text{ cm}^{-3} \quad (1)$$

$$n_{\text{ecav}} = (0.91r^{-23.6} + 2.33r^{-16.6} + 1.96r^{-6.81}) \times 10^8 \text{ cm}^{-3}, \quad (2)$$

where r is the altitude and r_{piv} is the altitude in the coordinate frame of the non-radial streamer, both in units of R_{\odot} . The streamer profile in Equation (1) is valid at the central axis of the streamer, and then merges into a spherically symmetric background with a Gaussian falloff in the manner described in Gibson et al. (2003).

In the altitude range of 1.05–1.20 R_{\odot} model streamer densities range from 4.1×10^8 (at the low-altitude limit) to $1.0 \times 10^8 \text{ cm}^{-3}$, and cavity densities range from 2.7×10^8 to $0.7 \times 10^8 \text{ cm}^{-3}$, values well within the range at which the lines we use are density insensitive. Fit-based uncertainties on these values (described in Paper II) are 15%–30%. More important than the fit uncertainties may be atomic-physics-based uncertainties related to the fit ratio. These are discussed in Section 3.4.

For this work we introduce a temperature variation in terms similar to the density variation, but with the temperature going to zero at the photosphere. This is numerically practical and not unreasonable given the low relative temperature of the photosphere:

$$T_{\text{str}} = S_0(r_{\text{piv}} - 1)^{S_1} + S_2(r_{\text{piv}} - 1)^{S_3} + S_4(r_{\text{piv}} - 1)^{S_5} \text{ MK} \quad (3)$$

$$T_{\text{cav}} = C_0(r - 1)^{C_1} + C_2(r - 1)^{C_3} + C_4(r - 1)^{C_5} \text{ MK}. \quad (4)$$

As for the density, the streamer profile in Equation (3) is valid at the central axis of the streamer, and then merges into the

background with a Gaussian falloff; the cavity temperature is entirely determined by Equation (4).

The intensity, $I(v_{ij})$, of an optically thin, collisionally dominated spectral line produced by iron at frequency v_{ij} and integrated along the line of sight, l , is given by

$$I = \frac{h\nu_{ij}}{4\pi} \int_{\text{los}} \frac{n_j(\text{Fe}^{+m})}{n(\text{Fe}^{+m})} \frac{n(\text{Fe}^{+m})}{n(\text{Fe})} \frac{n(\text{Fe})}{n(\text{H})} \frac{n(\text{H})}{n_e} \frac{A_{ji}}{n_e} n_e^2 dl, \quad (5)$$

where i, j are the lower and upper levels, A_{ji} is the spontaneous transition probability, $n_j(\text{Fe}^{+m})/n(\text{Fe}^{+m})$ is the number of ion Fe^{+m} at level j as a fraction of the number density of Fe^{+m} , $n(\text{Fe}^{+m})/n(\text{Fe})$ is the ionization ratio of the ion Fe^{+m} to the total number density of iron, $n(\text{Fe})/n(\text{H})$ is the abundance of iron relative to hydrogen, and $n(\text{H})/n_e$ is the abundance of hydrogen relative to free electrons (see Phillips et al. 2008). Most of these parameters can be included in a contribution function for each spectral line, $G(n_e, T)$, so that Equation (5) can be written as

$$I = \int_{\text{los}} G(n_e, T) n_e^2 dl, \quad (6)$$

where n_e is the electron density. We do not expect a significant radiative scattering component for the EUV lines we use at the altitudes we are considering in this work. For the lines we use here, the radiative scattering from disk radiation is negligible as are the indirect effects of photospheric radiation on the relevant ion populations.

We have selected lines for which the contribution function has very little density dependence, so the line intensity is effectively a function of n_e^2 . Changes in the overall magnitude of the density (i.e., multiplying it by a constant factor) are divided out of the temperature line ratio, but changes to the shape of the profile can alter the temperature results to some extent. We assume that the iron abundance and $n(\text{H})/n_e$ ratio are constant along the line of sight and would divide out of a line ratio.

The contribution function values, shown in Figure 3, were calculated using the Chianti database version 7.0 (Dere et al. 1997; Landi et al. 2012). We used the coronal abundances of Feldman et al. (1992), the Chianti ionization equilibrium

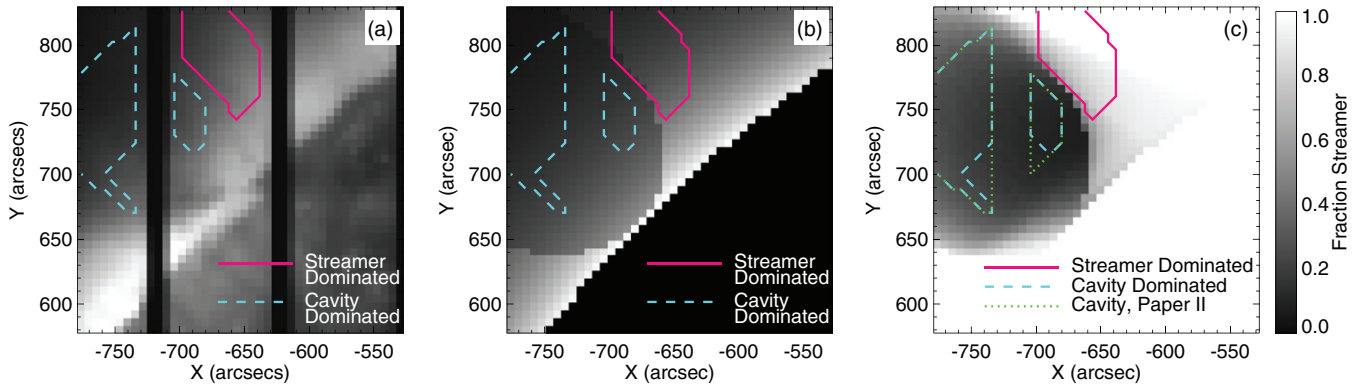


Figure 4. Location of the points designated “cavity” and “streamer” dominated in Figures 7, 9, and 10. These are superimposed on (a) the EIS Fe XII data and (b) the density in the plane of the sky from the morphological model (center). These points are not necessarily pure cavity or streamer along the line of sight, but tend to be dominated by emission from one region or the other. Panel (c) shows the fraction of emission from the streamer as opposed to the cavity at each pixel for a typical model fit. Panel (c) also shows the region used for the density modeling in Paper II.

(A color version of this figure is available in the online journal.)

calculations (Dere et al. 2009), and assumed a hydrogen to electron ratio of 0.83.

All lines used for the temperature analysis were deemed appropriate for emission measure analysis by Warren & Brooks (2009) except for the Fe XV 284.16 Å line. There were no indications of problems with that line, but there are no other lines in the EIS range with which it could be checked. We considered possible lines that might be blended with our main observational lines. We found that including the blend of the Si VII 274.18 Å line with the Fe XIV 274.20 Å line and Ar XI 184.52 Å with Fe X 184.54 Å led to detectable variations in our model intensities, and so included these fainter lines in the model calculations. However, these variations were small compared both to the uncertainties in the data and the model, so the inclusion of these lines does not affect our ultimate conclusions.

The pB is dependent only on electron density multiplied by a scattering function integrated along the line of sight, with no temperature component,

$$pB = \int_{\text{los}} n_e C(r) dl, \quad (7)$$

where $C(r)$ is a Thompson scattering function (Billings 1966; Fuller et al. 2008).

3.2. Temperature Ratio Analysis

In this paper, our primary task is to model the temperature of the cavity and streamer. By addressing the temperature ratios first before considering the model intensities, we focus on an observable quantity which isolates the effects of temperature and is relatively unaffected by density, filling factor, elemental abundances, or calibration errors.

In Figure 4, we show the regions used in the temperature analysis. These are very similar to those used in Paper II, but with a larger area around the prominence removed. Although it would be interesting to consider conditions in the prominence, the possible presence of Lyman absorption by the prominence would make the analysis difficult. The data for the density fit came from the larger area used in Paper II, but this affects the model density values by less than 10%.

The points are divided into “cavity” and “streamer” dominated areas, designating the main contributor to the emission from that point. However, each individual point may have both cavity and streamer contributions along the line of sight, as

shown in Figure 4(c). The POS altitude range for the points used is 1.050–1.163 R_\odot for the cavity area and 1.045–1.144 R_\odot for the streamer.

To analyze the data, we use an iterative procedure in which we used varying values of the parameters in Equations (3) and (4) to calculate model temperature profiles. These profiles were then used to calculate predicted line ratios of the lines listed in Table 1. Each line was divided by the line with the next hottest temperature of formation. Maps of the ratio data values are shown in Figure 5. Only the points within the contours shown were used for the analysis.

In addition to the temperature profile parameters, we found it necessary to introduce parameters designed to correct for uncertainties in atomic physics. It was clear from our initial fits to the data that there were some systematic difficulties in fitting the different ratios. These were consistent with uncertainties in the atomic data often considered to be as high as 20%, as discussed in Section 3.4. To counteract the effects of these uncertainties on our results we introduced variable parameters corresponding to a multiplicative factor for each of the line intensities. Although, for reasons discussed below, we are not able to calculate formal uncertainties for these parameters, we found that a factor of 0.8–0.9 applied to the model Fe XI 188.2 Å intensities dramatically improved the fits to the temperature ratios, while smaller corrections between 0.9–1.1 \pm 0.05 were indicated for the other lines.

A downhill simplex “amoeba” method (Nelder & Mead 1965) was used to determine the best fits. In this method a grid of possible solutions is calculated, and the best one is selected and used as a basis for a further grid of possible solutions until a stable optimized solution is determined. Our best-fit parameters are presented in Table 2. Figure 6 shows the model ratio maps corresponding to the data-based ratios in Figure 5. The model parameters in the temperature parameterization (Equations (3) and (4)) are not orthogonal and so this set of individual parameters is not necessarily unique. However, all good fits to the data converge toward the same actual temperature profiles. Figure 7 shows the corresponding data and model values as a function of altitude for each of the line ratios. In these plots the ratio value at each individual pixel in the analysis regions shown in Figure 4 is plotted as a function of altitude at that location, with the Poisson and dark current uncertainties shown for the data points. Although we distinguish in the plots between the points in regions in which the contribution

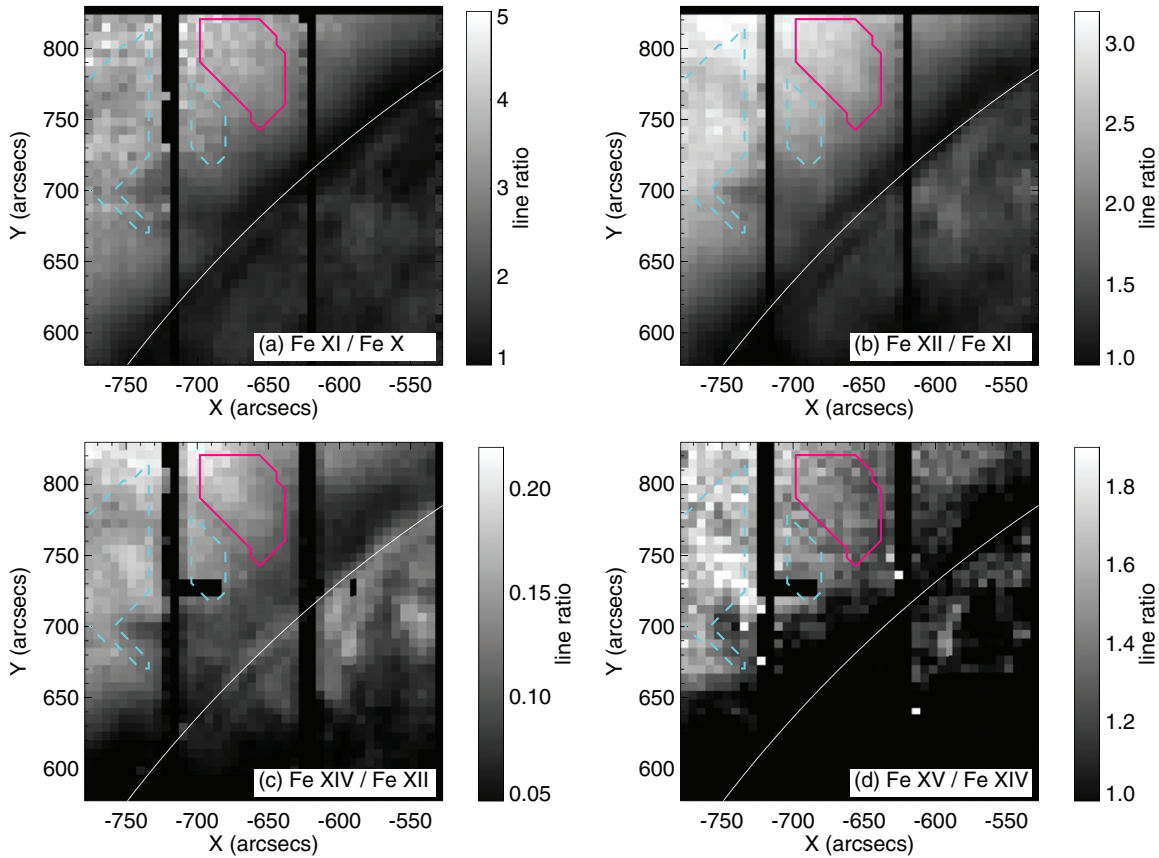


Figure 5. Maps of the EIS spectral line ratios. The area used to represent the cavity-dominated emission is shown by the dashed contour and the area representing the streamer-dominated emission is shown by the solid contour. The area shown with the black rectangle near $(-700'', 730'')$ is due to a data drop-out in the Fe XIV images and was not used in the ratios involving that line.

(A color version of this figure is available in the online journal.)

Table 2
Parameters in the Fit of Temperature-dependent Line Ratios

Streamer temp. parameters	S_0 : 1.378	S_1 : 0.150,	S_2 : -0.257	S_3 : 1.879	S_4 : 0.647	S_5 : 0.060
Cavity temp. parameters	C_0 : 1.181	C_1 : -0.255	C_2 : -0.143	C_3 : -0.768	C_4 : 0.304	C_5 : 0.031
Multiplicative factors for spectral lines	Fe x: 0.93	Fe xi: 0.83	Fe xii: 1	Fe xiv: 1.09	Fe xv: 1.08	

Notes. Parameters S_0 – S_5 are the parameters for the streamer temperature profile (Equation (3)) and C_0 – C_5 are the parameters for the cavity temperature profile (Equation (4)). The final row lists the multiplicative parameters for each spectral line intensity introduced to compensate for uncertainties in the atomic physics. These are normalized so that the factor for Fe XII is 1.

is streamer dominated or cavity dominated, all points were fit simultaneously.

It is difficult to determine the confidence level for these fits. Using only the Poisson and dark current uncertainties to the data points, the $\chi^2_v = 3.6$ is quite high. We think there are two main contributing factors to this. One is that there are significant systematic uncertainties that are hard to quantify as described in Section 3.4. For the temperature ratio many of these divide out, but there are uncertainties related to the scattered light removal and shape of the density profile that are not included in the uncertainties used in the fits. The other reason is that, particularly in the cavity, there are true variations in the line ratio data that are not adequately modeled using simple radial temperature profiles. These variations can be seen in both Figures 5 and 7. However, despite these factors, the

model seems to match the general variations with altitude fairly well, although there is a tendency for the model to underestimate the Fe XI/Fe X and Fe XII/Fe XI ratios in the streamer for altitudes $\gtrsim 1.10 R_\odot$.

In order to convey the sensitivity of the model fits we have shown in Figure 7 our best fit and also the model ratios for cases in which the temperatures in both the cavity and streamer were increased or decreased by 5%. This value is somewhat arbitrary, but produces changes in the model line ratios which are similar to the variation seen in the data.

In Figure 8(a), we show the model temperatures as a function of altitude along with the values of the best-fit temperature profiles $\pm 5\%$ for comparison with Figure 7.

In Figure 8(b), we have shown the effect of using different initial density profiles in our temperature fitting procedure.

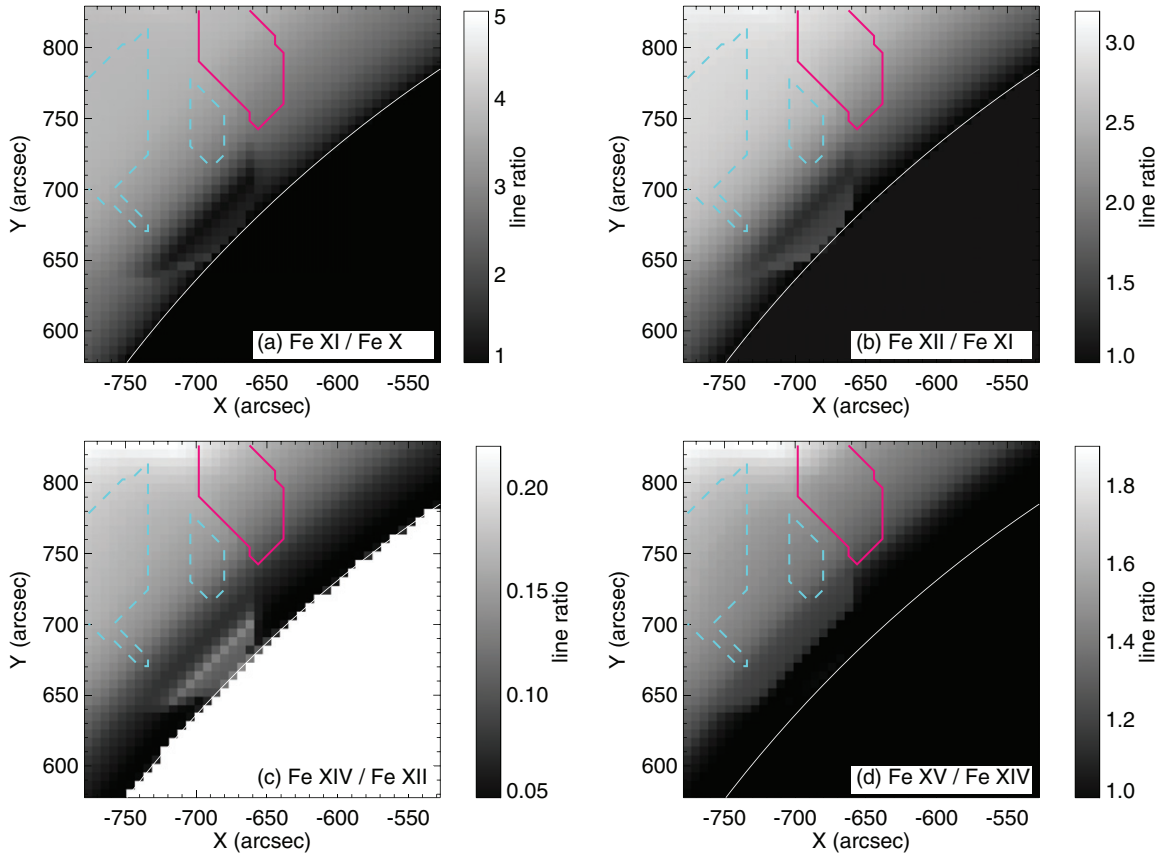


Figure 6. Maps of the model spectral line ratios. The area used to represent the cavity-dominated emission is shown by the dashed contour and the area representing the streamer-dominated emission is shown by the solid contour. The model temperatures at altitudes below these contours were not constrained by our fitting procedure. (A color version of this figure is available in the online journal.)

The density profiles used were the 90% confidence level uncertainties in the cavity densities for the isothermal model presented in Table 2 and Figure 5 of Paper II. The change in the temperature profile is in response to changes in slope in the density profile rather than changes in the magnitude of the density profile, which divides out of the line ratios.

3.3. Intensity Analysis

We also compared the model and data intensity, shown in Figure 9. We found that the ratio of the EIS line intensity data to the model is about 0.15 with a slight increase with altitude. This is in contrast to the pB data for which the model and data fit well.

In order to probe the possibility that the discrepancy is the result of a filling factor (see Section 4.2.1), we calculated new density profiles based on the EIS data alone. The density fit in Paper II was based on a combination of the EIS density-sensitive line ratios at altitudes below about $1.17 R_{\odot}$ and the MLSO pB data above that altitude, so it is to be expected that the pB data and the model fit well. If a density profile based on the density-sensitive Fe XII line ratio alone also overestimates the pB data, that would be consistent with the idea of a volume filling factor. We calculated the new EIS-only fit using data reduced as for the temperature analysis. Although these new density profiles in the cavity and streamer varied somewhat from the Paper II density profile, as much as 20% at lower altitudes, they still matched the Paper II curve and thus the pB data values well, with a pB data/model ratio of $1.0 \pm 10\%$ in the range 1.17 – $1.20 R_{\odot}$. The uncertainties are based on the

data uncertainties—calibration optics values, sky transmission, and pointing uncertainties as described by Elmore et al. (2003). This indicates that the discrepancy between the EUV model and data intensities is not due to a volume filling factor. We discuss other possible explanations for the discrepancy in Sections 3.4 and 4.2.

3.4. Uncertainties

As mentioned above, there are a number of uncertainties that are hard to quantify well enough to include in an analysis of the goodness of our fits. The advantage of using line ratios is that many uncertainties are removed or minimized in the division of the line intensities (see Section 3.1 and the discussion of Equations (5) and (6)). Of the uncertainties listed below only the uncertainties on the atomic parameters, the stray light, and the shape of the density profile are likely to effect the temperature-sensitive line ratio results significantly. All the uncertainties have the potential to affect the intensity calculations.

In general, uncertainties in spectral line intensities due to atomic physics are in the 20% range (e.g., Del Zanna 2010). We attempt to correct for these uncertainties to some extent with our line correction factor (see Table 2). A single correction for each line seems reasonable because of the relatively constrained range of temperatures and densities used in the model, but may not completely take care of any problems.

As discussed in Section 3, we have applied a stray light correction to these data. This is a rough estimate, however, so there is some amount of residual uncertainty related to stray light. To estimate how this may affect the data, we can compare

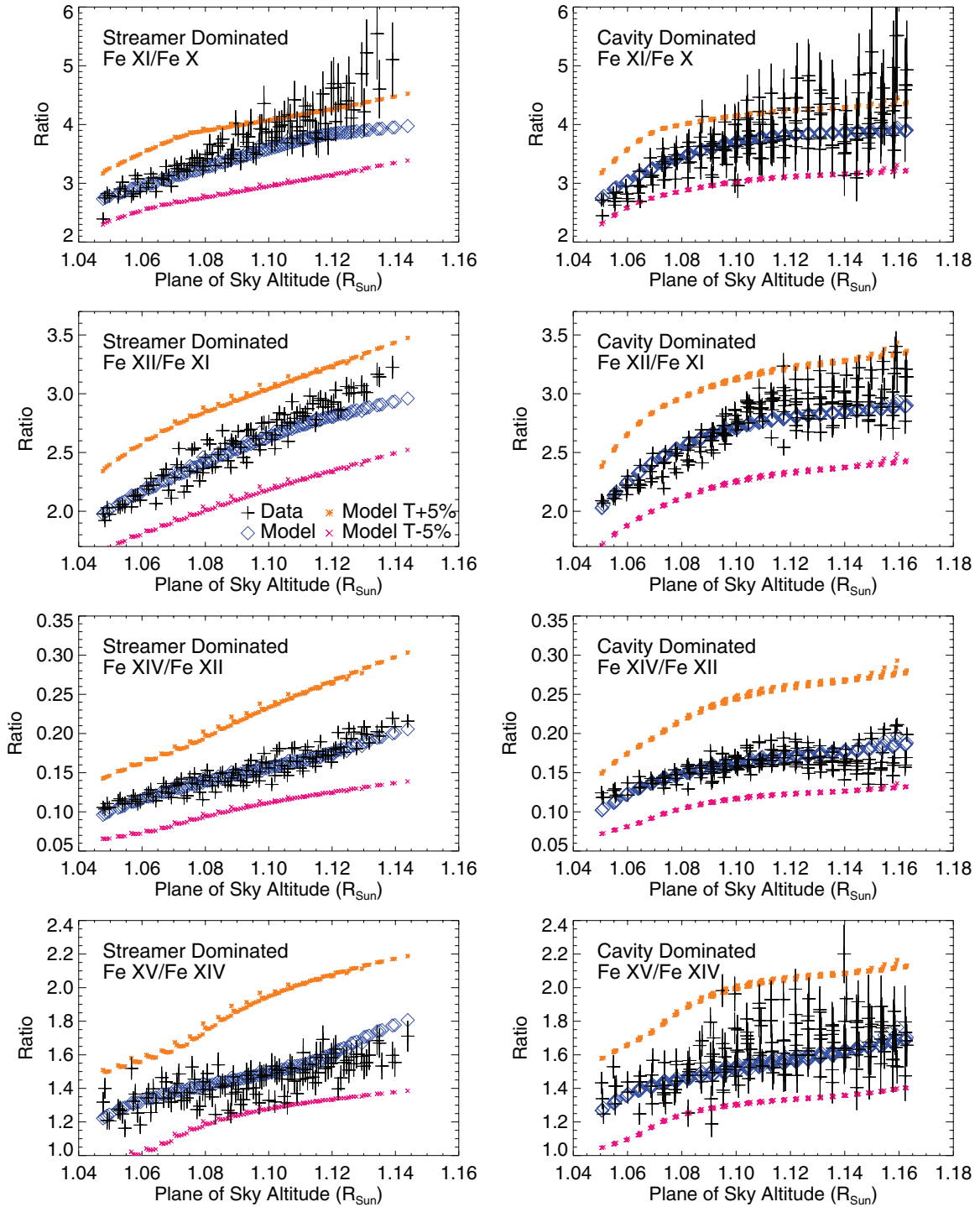


Figure 7. Line ratios vs. plane-of-sky altitude for data used for fit and model. The points in black are the data points corresponding to each data point in Figure 5 in regions outlined on that figure and Figure 4. The blue diamonds are the intensity values of the corresponding pixel as calculated with the model (Figure 6). The error bars on the data points represent Poisson and dark current uncertainties. The orange and pink points represent the model if both the cavity and streamer temperature profiles are increased (orange) or decreased (pink) by 5%.

(A color version of this figure is available in the online journal.)

the stray light corrected data to uncorrected data. The correction reduces the quality of the fit to the Fe XI/Fe X ratio at higher altitudes, but it does not affect the model temperature values greatly. In part this is because it is divided out somewhat in the line ratios so that the change in the Fe XI/Fe X ratio is less than 20% at $1.16 R_{\odot}$. Also, that ratio, which is most greatly affected by the stray light, is the one that has the greatest count-based uncertainties. An introduction of increased uncertainties

proportional to the stray light correction also does not greatly affect the fits.

Based on pre-flight calibrations (Lang et al. 2006), the uncertainties in the absolute radiometric calibration of EIS are 22%.

For the density values there are possible uncertainties associated with both the fitting procedure and the atomic physics. In Paper II, the estimated fit uncertainties (at a 90% confidence

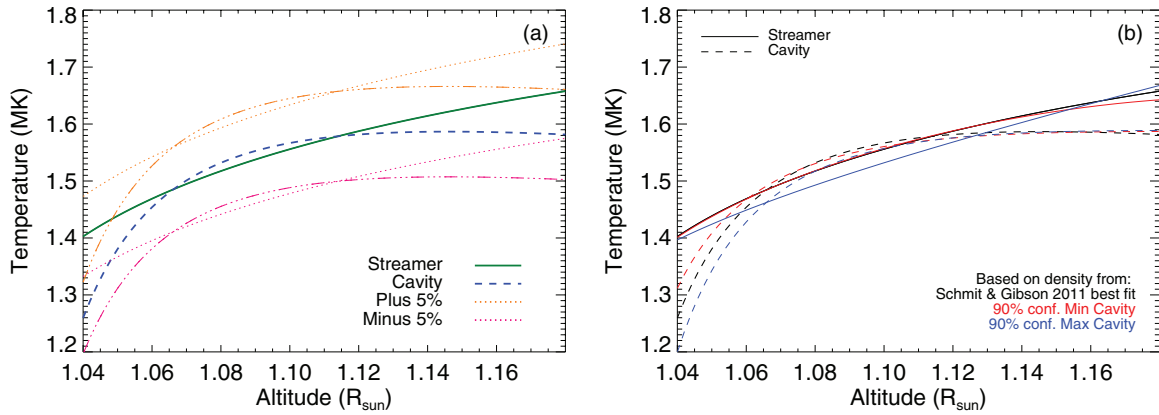


Figure 8. Temperature profiles as a function of r at the central longitude of the streamer corresponding to the fit parameters in Table 2. To provide an estimate of the uncertainties for these profiles, panel (a) includes curves showing the same temperature profiles $\pm 5\%$ for comparison with Figure 7 which shows the results of the model fits of a 5% variation in model temperature. In panel (b) we show a range of temperature fits based on the density fits in Table 2 of Paper II, corresponding to the best fits to the EIS and Mk4 data and maximum and minimum cavity densities based on 90% confidence levels. The curves show the result of refitting the temperature data using these density profiles. As mentioned in the text, variations in the average density value divide out of the temperature analysis, but the slopes of the density profiles have an effect on the temperature results.

(A color version of this figure is available in the online journal.)

level) of the cavity density are about 30% (at $1.17 R_{\odot}$) or better for lower altitudes. The streamer density uncertainties are thought to be 15% or better. As discussed in Section 3.2, we show the results of such variations on our temperature fits in Figure 8(b). As can be seen in the figure such variations in the density profile affect temperature curves somewhat, but do not change the overall results.

More important than the fit uncertainties are probably the uncertainties associated with the Fe XII 186.880/195.119 Å line ratio used to calculate the density. Warren & Brooks (2009) compared the results of various density diagnostics in the quiet corona, finding a variation in density of a factor of two. The Fe XII 186.880/195.119 Å ratio used in our density modeling was a factor of 1.12 higher than the average value considered most reliable. Young et al. (2009) compared densities calculated using the Fe XII 186.880/195.119 Å ratio with different Fe XIII-based ratios and found that the Fe XII-based densities averaged about 1.9 times higher than the Fe XIII-based values. Because the EUV intensities depend on the square of the density (Equation (6)), such an overestimation of the density could lead to an overestimation in the EUV model intensities by a factor as high as 3.6. Average, overall variations in the model density divide out of the temperature-dependent line ratios we use, so we do not expect these uncertainties to greatly affect the temperature results.

Another factor that should be considered is uncertainties in abundance values. In this investigation we are using abundance values derived from sources in the quiet portions of the lower corona (Feldman et al. 1992; Feldman 1992). For a low first ionization potential (FIP) element like iron such coronal abundances are thought to be approximately four times larger than abundances in the photosphere (Feldman & Widing 2002). However, Schmelz et al. (2012) have done an extensive review and recalculation based on new photospheric abundance measurements and find that the best estimate for the coronal abundance of iron is 1.8 times lower than the values we use, although they emphasize that the abundances probably vary. Other studies also suggest lower values for iron abundances. Spicer et al. (1998) present evidence that the abundances of low-FIP elements in prominences may be photospheric or midway between coronal and photospheric abundances. If this were the case and the

prominence plasma has condensed out of the hotter plasma of the cavity, then such abundances might also apply to the cavity. Warren & Brooks (2009) find in their study of the quiet corona that the Feldman et al. abundances may be overestimating the iron abundance by as much as a factor of 2.9. If we are indeed overestimating the iron abundance, it would not affect our modeling based on temperature-sensitive line ratios which use only iron lines, so that the abundances divide out. However, overestimations of the iron abundance values would affect the model EUV line intensities.

4. DISCUSSION

4.1. Streamer and Cavity Temperature

The fit to the general radial temperature trends indicates that the temperature in both the cavity and streamer ranges from about 1.4 MK at $1.04 R_{\odot}$ to about 1.6 MK in the range 1.14 – $1.16 R_{\odot}$ (Figure 8). There is some difference in the shape of the model profiles: the cavity temperature levels off around $1.10 R_{\odot}$, while the streamer temperature continues to rise. This should be considered, however, in light of the clear fine structure in the cavity temperatures, as discussed below.

In order to give an idea of the reliability of these results, we have added in Figure 8(a) curves showing the best temperature fit $\pm 5\%$. This is for comparison with Figure 7 in which the effects of such a change in the model temperatures are shown.

Numerous studies (e.g., Gibson et al. 1999; Feldman et al. 1999; Alexander 1999; Parenti et al. 2000, 2003) have analyzed temperatures of streamers at altitudes overlapping with those we consider. Temperature values are generally within 25% of those we measure here. Analysis of the same streamer can yield different results. For instance, Gibson et al. (1999) and Alexander (1999) analyzed the same streamer using an EUV line ratio and soft X-rays, respectively, and found that the temperatures derived from the X-ray data were 10%–20% higher than the EUV derived ones. Parenti et al. (2003) analyzed the same streamer with different line ratios and found differences in the resulting temperatures of 10%–30%. Generally, although not always (see Feldman et al. 1999), an increase with altitude is seen, usually with a somewhat more shallow slope ($\approx 1 \text{ MK } R_{\odot}^{-1}$)

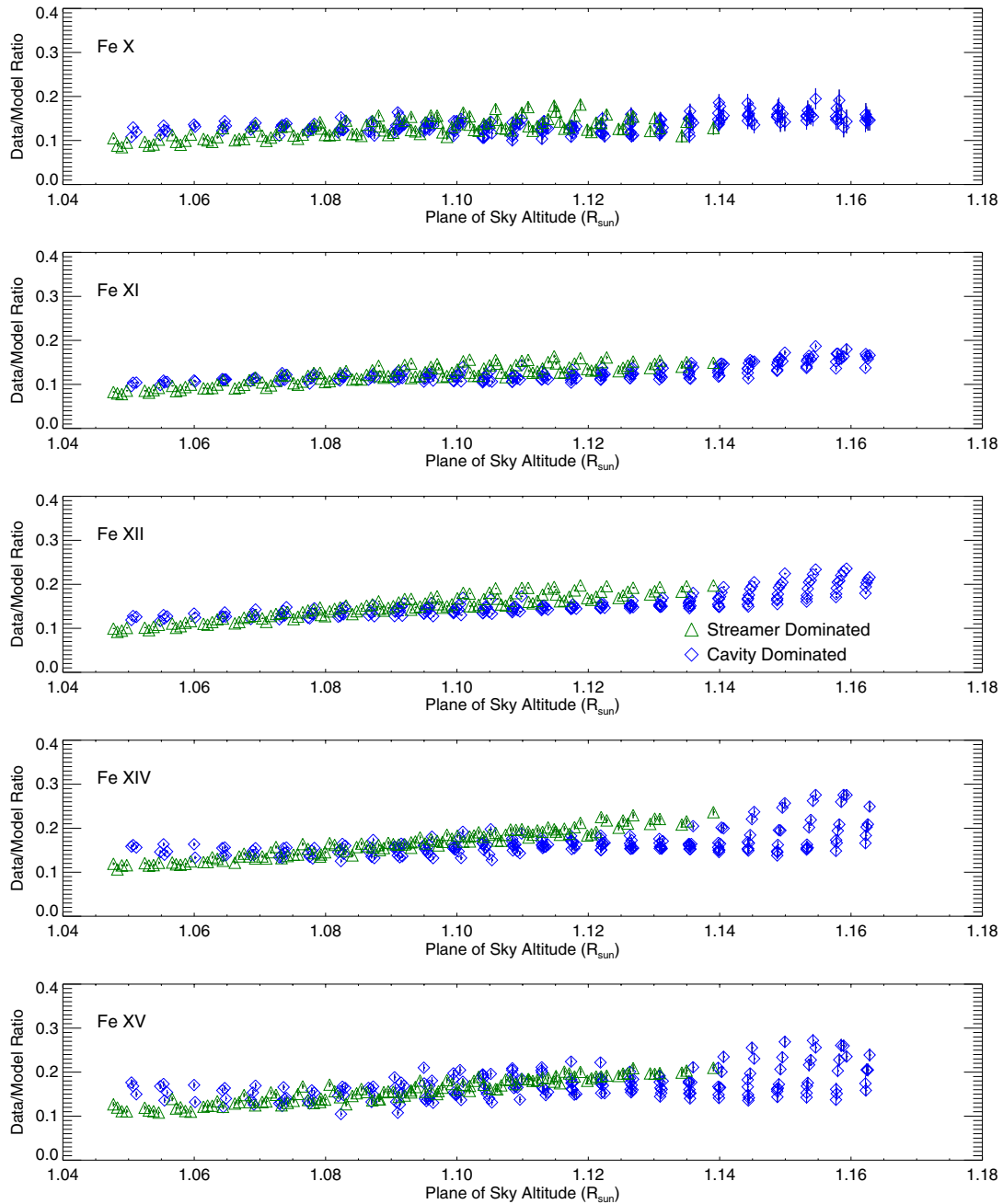


Figure 9. Ratio of the data and the model EUV line intensities vs. plane-of-sky altitude. Error bars shown are 1σ uncertainties based on the Poisson and dark current uncertainties of the EUV line intensity data. Not included are uncertainties related to EIS radiometric calibration, abundances, density, or scattered light.

(A color version of this figure is available in the online journal.)

than we see in our streamer temperature profile where the slope is close to $2 \text{ MK } R_{\odot}^{-1}$.

In addition to this radial increase, however, the cavity exhibits substructure variations. This is noticeable in the spread of values at a given altitude in the radial plots (Figures 7 and 10) and in structures apparent in the ratio images (Figure 5). In particular, the Fe XIV to Fe XII ratio shows two separate features at altitudes $\geq 1.14 R_{\odot}$. In Figure 7 it appears that the substructure increases with altitude, but this is partly because variations at lower altitudes that appeared to be connected to the prominence were removed because of possible contamination of the EUV intensities by Lyman absorption. Figure 10 is identical to Figure 7 except that the emission from the points in the extended

prominence (shown by the dashed contour in Figure 4(c)) has been added to show the lower altitude variations.

There have been earlier observations of temperature substructures within cavities. Hudson et al. (1999) and Reeves et al. (2012) reported hot features in coronal cavities observed in soft X-rays with *Yohkoh*/Soft X-ray Telescope (SXT) and *Hinode*/X-ray Telescope (XRT), respectively. In particular, Reeves et al. applied a version of the same forward model used in this analysis to a different cavity observed in 2008 July. It included no radial variation in temperature, but incorporated a source inside the cavity with enhanced density and temperature. Both direct analysis of the XRT data and forward modeling show that the data are consistent with a general cavity temperature of

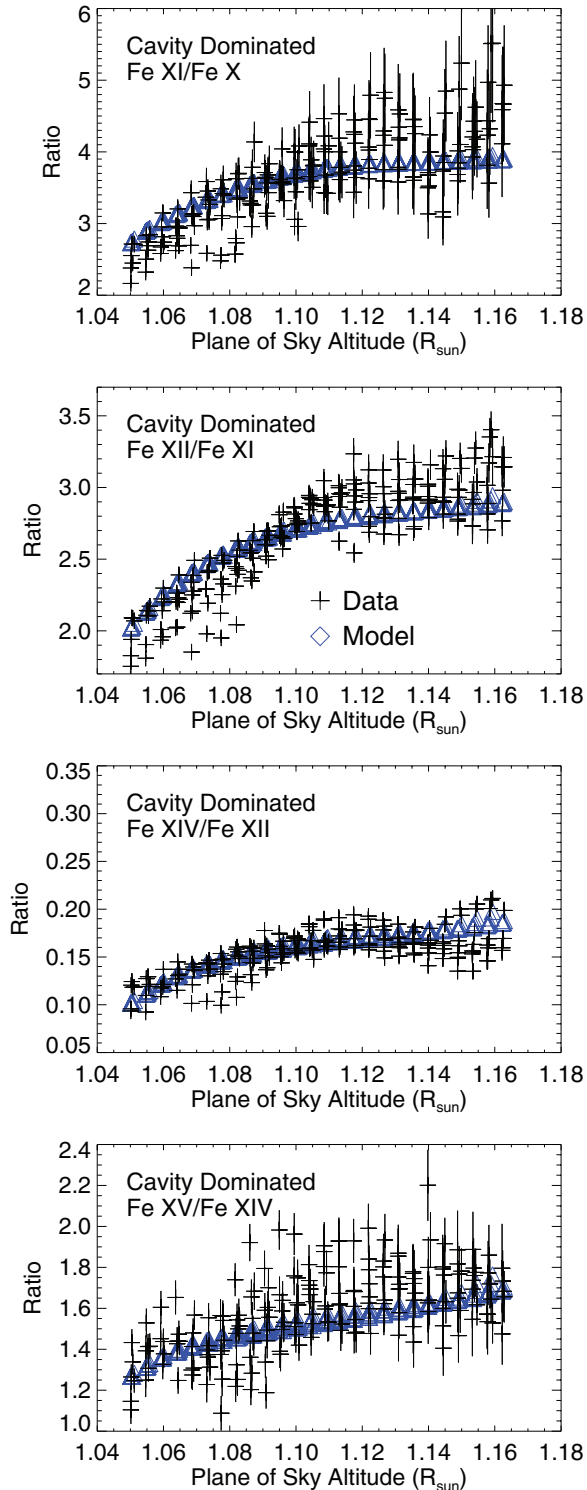


Figure 10. Line ratios vs. plane-of-sky altitude for data, including data near the prominence that were not used in the fit, and model (see Figure 4). The prominence data were taken out for the fitting in case the area exhibited Lyman absorption that might harm the results. Here we include them to show that the cavity substructure variations extend through a wide range of altitudes. The error bars on the data points represent 1σ Poisson and dark current uncertainties. (A color version of this figure is available in the online journal.)

1.4 MK plus a hot source with temperatures between 1.7 and 2.0 MK. The source showed substantial variation on scales of hours or less. In our case, we may have signs of a similar cavity substructure but without the localized high-temperature source that would make it more obvious.

Vásquez et al. (2009) used a tomographic technique applied to *STEREO*/EUVI images in the 171, 195, and 284 Å bands to analyze two streamers with cavities. They found a broader and hotter temperature distribution in the cavities than the streamers. We do not see any evidence for hotter plasma in the cavity than the streamer, although a broader temperature distribution might be consistent with cavity substructures that we do see in this study.

It is likely that such variations reveal magnetic structures in the cavity. In simulations performed by Luna et al. (2012), the footpoints of particular field lines in a sheared arcade model were subject to heating and the resulting motion and temperature variations along the field lines were calculated in terms of the thermal-nonequilibrium model (Karpen & Antiochos 2008, and references therein). The resulting end-on images, as in the case of a cavity on the limb, exhibit complex features in various temperatures following the twisted magnetic field lines in the cavity.

4.2. Line Intensities

Our observations are highly unusual in that we have access to three different quantities that provide information about the amount of material along the line of sight. We find that these three data sets do not give consistent results, so that model estimates of intensities based on densities determined from the EUV line ratios and the pB data are not consistent with the EUV intensity data, which the model overestimates by a factor of 4–10 that decreases with altitude. Here we discuss possible explanations for this discrepancy.

In order to understand the possible causes for this discrepancy, we need to consider how each of the data sets is produced: the density line ratio analysis provides information about densities in locations emitting in Fe XII lines; the EUV line intensities are dependent on iron abundance and n_e^2 integrated along the line of sight (see Equation (5)), while the pB values are dependent on n_e integrated along the line of sight (Equation (7)).

4.2.1. Filling Factor

In our model, we assume a smoothly varying density profile (except for a discontinuity at the cavity–streamer boundary). This may not actually be the case. In fact, our temperature results indicate that the cavity in particular is not very smooth, suggesting the possibility that a filling factor may be affecting our results.

Comparisons of EUV intensity and line ratio data have been used in the past to determine filling factors. The Fe XII line ratio is only sensitive to densities in areas with sufficient density and at about 10^6 K. The EUV intensity, on the other hand, is integrated over the entire line of sight and would, as a result, be lowered by an introduction of a filling factor in the model such that portions of the modeled volume were not producing emission from Fe XII. Filling factors on the order of 0.1 or even smaller have been recorded in active region loops (e.g. Warren et al. 2008; Tripathi et al. 2009) and prominences (e.g., Mariska et al. 1979; Kucera et al. 1998; Chiuderi Drago et al. 2001).

However, in our case the model is consistent with the pB data at altitudes near where the two data sets almost overlap ($\approx 1.17 R_\odot$), even when the density profile used is derived from the EIS line ratio data alone (see Section 3.3). This makes a volume filling factor any smaller than about 0.9 very unlikely at that altitude. We also considered the possibility of a temperature-based filling factor, such that there was a significant amount of material at temperatures outside the range observed by the EIS

lines we used ($\log T(\text{K})$ of 5.9–6.6) and thus not contributing to the EUV emission but still contributing to the pB, which is dependent on density alone. However, it seems unlikely that this could explain most of the discrepancy. That would require an amount of material at other temperatures sufficient to be detected in observations of cooler and hotter plasmas, which is not observed.

Thus, we think the role of a density- or temperature-based filling factor is limited. A filling factor could be responsible for the greater discrepancy observed at lower altitudes, but could only be making a relatively small contribution to the EUV data to discrepancy at altitudes near the upper altitude limit of the EIS data, $1.17 R_{\odot}$.

4.2.2. Uncertainties in the Model EUV Emission

As discussed in Section 3.4, there are some significant uncertainties in the modeling of the EUV emission. Measurements in the literature are consistent with iron abundances of 2 or even 3.9 times less than the ones we are using. A change in the abundance value used would not affect the pB model and its agreement with the data at all. If the Fe XII 186.880/195.119 Å density diagnostic is indeed overestimating the density then a correction could result in a reduction in the model EUV intensities by a factor of 3–4 while reducing the pB model intensities of 1.5–2. Thus, these uncertainties in parameters incorporated into the EUV intensity model, especially the abundance, are good candidates to explain the discrepancy between the EUV model and data. Uncertainties in the data calibration may factor in as well. We note that all these uncertainties divide out of a line ratio either entirely or to a great extent and so do not significantly affect our results based on temperature-sensitive line ratios.

4.3. Prominence

The focus of this paper is the prominence cavity rather than the prominence itself. The prominence may be viewed as a tightly coupled part of the prominence cavity, but one that presents different analysis challenges because of its cool, dense plasma that results in emission in lines that can be optically thick and include radiatively scattered components and Lyman continuum absorption in the EUV. Thus, a detailed analysis is beyond the scope of this paper. Still, we can make some observations about the properties of the prominence itself. The extents of the prominence in EIT 304 Å and the EIS Fe VIII are similar; it is more extensive in these lines than in the Lyman absorption seen in the Fe XII 195.1 Å line. The Fe VIII line response peaks at $\log T(\text{K}) = 5.7$ and it frequently exhibits prominence emission (e.g., Labrosse et al. 2011).

We also note that there is prominence emission in both the Fe X 184.5 Å and Fe XI 188.2 Å lines, indicating that there is material at even hotter temperatures in the prominence–corona transition regions (PCTR). The presence of such emission should be taken into account in attempts to model the PCTR. Searching through the Chianti database, we have not found any line blends with cooler lines that are likely to be contributing to this emission. Conversely, the Fe XIV 274.1 Å and Fe XV 284.2 Å lines show a lack of emission in areas in which there is emission at lower temperatures, particularly in the area near ($-730''$, $700''$) in Figure 1. This could be due to a lack of relatively high temperature emission, but it is also possible there is a contribution from Lyman absorption, which would be different for 274–285 Å than in the 185–195 Å range (see Heinzel et al. 2008).

5. SUMMARY AND CONCLUSIONS

Building on earlier forward modeling of this cavity and streamer to determine geometry and density profiles (Gibson et al. 2010; Schmit & Gibson 2011), we use temperature-dependent ratios of iron lines observed with *Hinode*/EIS to constrain cavity and streamer temperature. We find that a fit to the data with an altitude-dependent temperature profile indicates that both the streamer and cavity have temperatures in the range 1.4–1.7 MK, consistent with earlier measurements of streamer temperatures. However, the data clearly show significant temperature substructure in the cavity that cannot be described with a simple function of radius. This is consistent with other observations of significant substructure in cavities evident in hot cavity sources (Hudson et al. 1999; Reeves et al. 2012) and velocity signatures (Schmit et al. 2009; Wang & Stenborg 2010). It seems likely that these structures are projections of cavity magnetic field with varying plasma conditions between and perhaps along different magnetic field lines in the cavity. Understanding such structures may be a key to determining the magnetic field structure of the cavity and thus the entire pre-CME magnetic configuration.

We find that the model, although consistent with the EUV density and temperature-sensitive line ratios, overestimates the EUV line intensity by a radially decreasing factor of 10–4. However, the pB model and data at the altitudes at which the EUV and pB data nearly overlap are consistent even when the density profile is calculated entirely independently of the pB data using the only EIS density-sensitive line ratios. This indicates that filling factor is unlikely to be an important factor at the high-altitude limit of the EUV range. Instead, we suggest that the discrepancy is the result of documented uncertainties in the Fe XII 186.880/195.119 Å line diagnostic and, especially, the iron abundance used in the model. The uncertainties in these factors are sufficient to explain a factor of four discrepancy in the model at the high-altitude limit of the EIS data, without greatly affecting the agreement of the pB data and model. A filling factor may also play a role at lower altitudes.

The authors thank the International Space Science Institute (ISSI) for funding a Working Group on Coronal Cavities, where this work began. We thank Judy Karpen, Jim Klimchuk, Adrian Daw, and Jack Ireland for helpful conversations and Judy Karpen also for useful comments on the manuscript. We thank the referee whose comments and questions led to a substantially improved paper. T.K. was supported by a grant from the NASA SHP program; E.L. by the NNX10AM17G, NNX11AC20G, and other NASA grants; and D.S. by the NASA Earth and Space Science Fellowship program. *Hinode* is a Japanese mission developed and launched by ISAS/JAXA, with NAOJ as domestic partner and NASA and STFC (UK) as international partners. It is operated by these agencies in cooperation with ESA and NSC (Norway). *SOHO* is a mission of international cooperation between ESA and NASA. The National Center for Atmospheric Research is sponsored by the National Science Foundation. Chianti is a collaborative project involving George Mason University, the University of Michigan (USA), and the University of Cambridge (UK).

Facilities: *Hinode* (EIS), *SOHO* (EIT), HAO (MLSO/Mk4)

REFERENCES

- Alexander, D. 1999, *J. Geophys. Res.*, **104**, 9701
- Billings, D. E. 1966, *A Guide to the Solar Corona* (New York: Academic)

- Chiuderi Drago, F., Alissandrakis, C. E., Bastian, T., Bocchialini, K., & Harrison, R. A. 2001, *Sol. Phys.*, **199**, 115
- Culhane, J. L., Harra, L. K., James, A. M., et al. 2007, *Sol. Phys.*, **243**, 19
- Del Zanna, G. 2010, *A&A*, **514**, A41
- Dere, K. P., Landi, E., Mason, H. E., Monsignori Fossi, B. C., & Young, P. R. 1997, *A&AS*, **125**, 149
- Dere, K. P., Landi, E., Young, P. R., et al. 2009, *A&A*, **498**, 915
- Elmore, D. F., Burkepile, J. T., Darnell, J. A., Lecinski, A. R., & Stanger, A. L. 2003, *Proc. SPIE*, **4843**, 66
- Feldman, U. 1992, *Phys. Scr.*, **46**, 202
- Feldman, U., Doschek, G. A., Schühle, U., & Wilhelm, K. 1999, *ApJ*, **518**, 500
- Feldman, U., Mandelbaum, P., Seely, J. F., Doschek, G. A., & Gursky, H. 1992, *ApJS*, **81**, 387
- Feldman, U., & Widing, K. G. 2002, *Phys. Plasmas*, **9**, 629
- Fuller, J., & Gibson, S. E. 2009, *ApJ*, **700**, 1205
- Fuller, J., Gibson, S. E., de Toma, G., & Fan, Y. 2008, *ApJ*, **678**, 515
- Gibson, S. E., Fludra, A., Bagenal, F., et al. 1999, *J. Geophys. Res.*, **104**, 9691
- Gibson, S. E., Foster, D., Burkepile, J., de Toma, G., & Stanger, A. 2006, *ApJ*, **641**, 590
- Gibson, S. E., Foster, D. J., Guhathakurta, M., Holzer, T., & St. Cyr, O. C. 2003, *J. Geophys. Res. (Space Phys.)*, **108**, 1444
- Gibson, S. E., Kucera, T. A., Rastawicki, D., et al. 2010, *ApJ*, **724**, 1133
- Guhathakurta, M., Rottman, G. J., Fisher, R. R., Orrall, F. Q., & Altrock, R. C. 1992, *ApJ*, **388**, 633
- Habbal, S. R., Druckmueller, M., Morgan, H., et al. 2010, *ApJ*, **719**, 1362
- Hahn, M., Landi, E., & Savin, D. W. 2011, *ApJ*, **736**, 101
- Heinzel, P., Schmieder, B., Fárnik, F., et al. 2008, *ApJ*, **686**, 1383
- Hudson, H. S., Acton, L. W., Harvey, K. L., & McKenzie, D. E. 1999, *ApJ*, **513**, L83
- Karpen, J. T., & Antiochos, S. K. 2008, *ApJ*, **676**, 658
- Kucera, T. A., Andretta, V., & Poland, A. I. 1998, *Sol. Phys.*, **183**, 91
- Labrosse, N., Schmieder, B., Heinzel, P., & Watanabe, T. 2011, *A&A*, **531**, A69
- Landi, E., Del Zanna, G., Young, P. R., Dere, K. P., & Mason, H. E. 2012, *ApJ*, **744**, 99
- Lang, J., Kent, B. J., Paustian, W., et al. 2006, *Appl. Opt.*, **45**, 8689
- Luna, M., Karpen, J. T., & DeVore, C. R. 2012, *ApJ*, **746**, 30
- Mariska, J. T., Doschek, G. A., & Feldman, U. 1979, *ApJ*, **232**, 929
- Nelder, J. A., & Mead, R. 1965, *Comput. J.*, **7**, 308
- Parenti, S., Bromage, B. J. I., Poletto, G., et al. 2000, *A&A*, **363**, 800
- Parenti, S., Landi, E., & Bromage, B. J. I. 2003, *ApJ*, **590**, 519
- Phillips, K. J. H., Feldman, U., & Landi, E. 2008, *Ultraviolet and X-Ray Spectroscopy of the Solar Atmosphere* (Cambridge: Cambridge Univ. Press)
- Reeves, K. K., Gibson, S. E., Kucera, T. A., Hudson, H. S., & Kano, R. 2012, *ApJ*, **746**, 146
- Schmelz, J., Reames, D., von Steiger, R., & Basu, S. 2012, *ApJ*, **755**, 33
- Schmit, D. J., & Gibson, S. E. 2011, *ApJ*, **733**, 1
- Schmit, D. J., Gibson, S. E., Tomczyk, S., et al. 2009, *ApJ*, **700**, L96
- Spicer, D. S., Feldman, U., Widing, K. G., & Rilee, M. 1998, *ApJ*, **494**, 450
- Tripathi, D., Mason, H. E., Dwivedi, B. N., del Zanna, G., & Young, P. R. 2009, *ApJ*, **694**, 1256
- Ugarte-Urra, I. 2010, *EIS Software Note 12*, version 1.0
- Vázquez, A. M., Frazin, R. A., & Kamalabadi, F. 2009, *Sol. Phys.*, **256**, 73
- Wang, Y.-M., & Stenborg, G. 2010, *ApJ*, **719**, L181
- Warren, H. P., & Brooks, D. H. 2009, *ApJ*, **700**, 762
- Warren, H. P., Ugarte-Urra, I., Doschek, G. A., Brooks, D. H., & Williams, D. R. 2008, *ApJ*, **686**, L131
- Young, P. 2011, *EIS Software Note 1*, version 3.3
- Young, P. R., Watanabe, T., Hara, H., & Mariska, J. T. 2009, *A&A*, **495**, 587